

## Applied Catalysis A General 505 (2015) 467-477

<http://dx.doi.org/10.1016/j.apcata.2015.05.011>

### **Boosting the visible-light photoactivity of $\text{Bi}_2\text{WO}_6$ using acidic carbon additives**

Rocio J. Carmona<sup>1</sup>, Leticia F. Velasco<sup>2</sup>, M. Carmen Hidalgo<sup>3</sup>, José A. Navío<sup>3</sup>, Conchi O. Ania<sup>1\*</sup>

<sup>1</sup>ADPOR Group, Instituto Nacional del Carbón (INCAR), Consejo Superior de Investigaciones Científicas (CSIC), Apdo. 73, 33080 Oviedo, Spain

<sup>2</sup>Dpt. Chemistry, Royal Military Academy, Renaissancelaan 30, 1000 Brussels, Belgium

<sup>3</sup>Instituto de Ciencia de Materiales de Sevilla (ICMS), Consejo Superior de Investigaciones Científicas (CSIC) - Universidad de Sevilla, Américo Vespucio 49, 41092 Sevilla, Spain

\*-Corresponding author. Tel.: +34 985 118846. Fax: +34 985297662. E-mail address: [conchi.ania@incar.csic.es](mailto:conchi.ania@incar.csic.es) (CO Ania).

**Abstract**

We have explored the role of the physicochemical properties of carbon materials as additives to bismuth tungstate on its structure, optical properties, and photocatalytic activity for the degradation of rhodamine B under visible light. For this purpose, C/Bi<sub>2</sub>WO<sub>6</sub> hybrid composites were prepared following two different routes: i) physical mixture of the catalyst components, and ii) one-pot hydrothermal synthesis of the semiconductor in the presence of the carbon additive. Three carbons with different properties were selected as additives: biomass-derived activated carbon, carbon nanotubes and carbon spheres obtained from polysaccharides. Data has shown the outstanding role of the acidic/basic nature of the carbon additive, and of the synthetic method on the photocatalytic performance of the resulting composites. For a given additive, the degradation rate of RhB is greatly improved for the catalysts prepared through a one-step hydrothermal synthesis, where there is low shielding effect of the carbon matrix. Carbon additives of acidic nature boost the surface acidity of the hybrid photocatalyst, thereby enhancing the photodegradation of RhB under visible light via a coupled mechanism (photosensitization, semiconductor photocatalysis and carbon-photon mediated reactions).

Keywords: nanoporous carbons, heterogeneous photocatalysis, visible light, bismuth tungstate

## 1. Introduction

Triggered by the low photonic efficiency of common semiconductors under visible light, many research efforts are currently being conducted on developing novel photocatalysts with enhanced activity, aiming at achieving a more efficient use of sunlight for its application in several fields such as environmental remediation or energy conversion [1,2]. Among others, bismuth-based materials and particularly  $\text{Bi}_2\text{WO}_6$  have revealed as suitable alternatives to widespread used  $\text{TiO}_2$  [3-5].  $\text{Bi}_2\text{WO}_6$  has a layered structure with perovskite-like slabs of  $\text{WO}_6$  and  $[\text{Bi}_2\text{O}_2]^{2+}$  layers, shows good light absorption properties in the visible range and has been found to present good photocatalytic activity for organic compounds and dyes degradation under visible light irradiation [4-7]. However, the physical features of  $\text{Bi}_2\text{WO}_6$  (surface area, morphology, particle size, crystallinity) and hence its photoactivity and stability under illumination are strongly affected by the synthesis method [4-7], constituting a major drawback of this material. Thus, improving its photocatalytic activity and stability is still needed to efficiently exploit its potentialities.

On the other hand, carbon materials have been successfully used -either as additives or porous supports to semiconductors- in a number of photoassisted reactions [8-10]. Carbon/semiconductor composites display superior photocatalytic performance than bare semiconductors, and overcome the operational drawbacks associated to the recovery and reuse of nanosized catalyst powders [11]. The origin of the increased photoconversion yields of carbon/semiconductor catalysts depends on the nature of the carbon additive (e.g., nanoporous carbons, nanotubes, graphene), and has been mostly discussed in terms of: i) the enhanced visible light absorption of the carbon component, ii) an enhanced mass transfer due to adsorption in the porous support, and iii) strong interfacial electronic effects between certain carbon nanostructures and the semiconductor [8-10].

Recent investigations including our own have reported that the photocatalytic performance of  $\text{Bi}_2\text{WO}_6$  can be enhanced by the use of certain amounts of carbon additives [12,13], although the effect of the carbon component has been barely addressed. Also, we have recently demonstrated the intrinsic photoactivity of several semiconductor-free nanoporous carbons under UV and visible light [14,15], and their ability to photogenerate O-radicals as the key aspect to achieve high photooxidation conversions of pollutants in aqueous solution [16].

Knowing this, the objective of this work was to provide a deep insight in the photocatalytic performance of hybrid  $\text{Bi}_2\text{WO}_6$ /carbon composites by exploring the role of the carbon additive. The novelty of this work is to clarify the effect of the characteristics of the carbon additive, in terms of structure, porosity and surface chemistry. Our results provide new insights on the photodegradation mechanism of a dye using  $\text{Bi}_2\text{WO}_6$ /carbon catalysts, and highlight the outstanding importance of the synthetic route followed for the incorporation of the carbon additive on the performance of the composite.

To achieve this goal our approach consisted on the synthesis of carbon/ $\text{Bi}_2\text{WO}_6$  composites using carbon materials with different physicochemical properties (nanotubes, spheres and nanoporous carbon). All of them are also characterized by a non-negligible intrinsic photochemical activity under UV light [15,17,18]. To obtain a deeper knowledge of the C/ $\text{Bi}_2\text{WO}_6$  composites, catalysts were prepared following two different approaches: i) physical mixture of the components, and ii) through a one-pot route consisting on carrying out the hydrothermal synthesis of  $\text{Bi}_2\text{WO}_6$  in the presence of the carbon additive. Rhodamine B was selected as model compound representing a recalcitrant dye frequently found in wastewater.

## **2. Experimental**

### *2.1. Materials synthesis*

$\text{Bi}_2\text{WO}_6$  (BWO) was prepared by following a hydrothermal procedure described elsewhere [12]. Briefly, about 0.01 mol of  $\text{Bi}(\text{NO}_3)_3 \cdot 5\text{H}_2\text{O}$  were dissolved in 10 mL of glacial acetic acid, and the stoichiometric amount of the tungsten precursor (0.005 mol of  $\text{Na}_2\text{WO}_4 \cdot 2\text{H}_2\text{O}$ ) were dissolved in 90 mL of distilled water. These two solutions were finally mixed to form a white suspension ( $\sim\text{pH } 2$ ), kept under stirring for 30 min, and then transferred into a Teflon lined stainless steel autoclave. The hydrothermal treatment was performed at 140 °C for 20 h. The yellowish precipitate was then filtered, repeatedly washed and dried overnight at 120 °C. An aliquot of the powders was calcined at 300 °C for 4 h (labeled as calc).

For the preparation of the composites, a weight ratio of 2% was selected based on our previous studies [12]. As mentioned, two synthetic approaches were envisaged for the incorporation of the carbon additive to the semiconductor: i) physical mixture of the carbon and  $\text{Bi}_2\text{WO}_6$  powders (series PM) in a mortar, and ii) through a one-pot route adding the carbon material to the precursors mixture for the preparation of  $\text{Bi}_2\text{WO}_6$  (series HS). For the latter, the suspension of carbon material + BWO precursors was sonicated for 15 min and kept under stirring for other 15 min to allow a good dispersion before the hydrothermal treatment. The obtained powders displayed from brownish to grey color depending on the nature of the carbon additive and on the synthesis conditions (Figure 1). The hybrid composites were labeled as BWO/X -being X the corresponding acronym of the carbon material used as additive-, followed by the indication of the synthetic route (either PM or HS).

The catalysts of the HS series were neither calcined (in air) nor annealed (inert atmosphere) above 120°C, to avoid modifications of the carbon component arising from burning-out and/or oxidation reactions. Indeed, it is well known that carbon materials prepared through a low temperature profile (i.e., sample CS) are very prone to oxidation in air at temperatures above 200°C, and that the composition of highly functionalized carbons (i.e., samples CL and CS)

can be easily modified upon thermal annealing (see Figure S1 in the Electronic Supporting Information, ESI).

Several carbon additives with varied physicochemical and structural characteristics were selected in this study: a nanoporous activated carbon prepared by chemical activation of a lignocellulosic precursor (sample CL), carbon spheres prepared by hydrothermal carbonization of polysaccharides (sample CS), and commercially available multiwall carbon nanotubes (sample CNT, Nanocyl, average nanotubes diameter 9.5 nm, average length 1.5 mm, carbon purity was 90%; see also [www.nanocyl.com](http://www.nanocyl.com)). Further details on the carbon additives (Raman and XRD spectroscopies) are compiled in Table 1 and Figures S2 and S3.

In a typical synthesis of the carbon spheres, about 250 mL of 0.5 M glucose solution was placed in a 400 mL Teflon-lined autoclave, and maintained at 180 °C for 10 hours to allow hydrothermal carbonization of the polysaccharide. The brownish solid obtained was isolated from the solution by centrifugation, washed several times with water and ethanol and dried at 60 °C. All the carbon materials were previously washed in distilled water in order to eliminate impurities. Selected characteristics of the carbon materials are shown in Table 1.

## 2.2. Characterization of the catalysts

The porosity of the samples was characterized by measuring the N<sub>2</sub> adsorption isotherms at -196 °C in a volumetric analyzer (ASAP 2020, Micromeritics). Before the experiments, the samples were outgased under vacuum (ca. 10<sup>-3</sup> torr) at 120 °C overnight. The isotherms were used to calculate the specific surface area,  $S_{\text{BET}}$  and total pore volume,  $V_{\text{total}}$ ; micropore volume was analyzed using the Dubinin–Radushkevich formulism ( $V_{\text{micro}}$ ) [19]. Elemental analysis was carried out in LECO CHNS-932 and LECO VTF-900 automatic analyzers. The hydrophobic/hydrophilic nature of the materials was characterized by the determination of the surface pH and proton binding curves by potentiometric titration. Briefly, subsamples of the

initial materials (~ 0.125 g) were added to NaNO<sub>3</sub> (10mM, 50 mL) and equilibrated under stirring overnight. The suspensions are acidified in 0.1M HCl until pH 3 and titrated with 0.1 M NaOH up to pH 11 using an automatic analyzer. During the titration the suspension was purged with N<sub>2</sub> to eliminate the influence of atmospheric CO<sub>2</sub>. The experimental data was transformed into proton binding curves, Q(H<sup>+</sup>), representing the total amount of protonated sites [20]. The morphology of the samples was characterized by scanning electron microscopy recorded using a FE-SEM apparatus (QuantaSEM, FEI), with metallic coating of the samples to obtain high quality images. The crystalline phase composition and degree of crystallinity of the samples were estimated by X-ray diffraction (XRD), using a Bruker instrument (D8 Advance) operating at 40 kV and 40 mA and using CuK $\alpha$  (0.15406 nm) radiation. Crystallite sizes of the different phases were estimated from the line broadening of the corresponding XRD peaks by using the Scherrer equation  $\tau = 0.9\lambda/\beta\cos\theta$ , where  $\lambda$  is the wavelength of the incident X-rays,  $\beta$  is the full width at half maximum height in radians, and  $\theta$  is the diffraction angle. The optical features of the catalysts were determined by UV-Vis diffuse reflectance spectroscopy, recorded on a Shimadzu spectrometer (UV-2501) equipped with an integrating sphere and using BaSO<sub>4</sub> as a blank reference. Measurements were recorded in the diffuse reflectance mode (R) and transformed to a magnitude proportional to the extinction coefficient through the Kubelka-Munk function, F(R $\infty$ ).

X-ray photoelectron spectroscopy (XPS) measurements were carried out in a SPECS spectrometer, using Mg K $\alpha$  radiation (150 W, 10 kV, 1253.6 eV) and a multichannel detector for the analysis of the core level signals of Bi 4f, W 4f, O 1s and C 1s. Binding energies for the high resolution spectra were calibrated by setting C 1s to 284.6 eV. CasaXPS software package was used for acquisition and data analysis; during data processing, a Shirley-type background correction was applied to the signal, and recorded spectra were fitted using Gauss-Lorentz functions, in order to determine the binding energy of the different element

core levels more accurately. The assignment of the distinct surface groups was performed upon the binding energies according to literature [21].

### *2.3. Photodegradation runs*

The photocatalytic activity of the samples was evaluated towards Rhodamine B (RhB) photooxidation in water using a batch reactor (250 mL) illuminated with an Osram Ultra-Vitalux lamp (300 W) with sunlike radiation spectrum (the incident photon flux on the solution as measured by chemical actinometry [22] was  $3.7 \times 10^{-6}$  einsteins/s). All prepared catalysts were gently homogenized in a mortar before being dispersed into the solution. Before each experiment, a catalysts loading of 1 g/L was settled in suspension with a RhB solution and allowed to equilibrate under stirring and darkness until no further adsorption took place (between ca. 2-12 hours), and hence the concentration of RhB from solution was constant (ca. 10 ppm). A constant oxygen flow of ca. 35 L/h was maintained in the solution during the photocatalytic runs. The photocatalytic reaction was followed by the evolution of RhB concentration and N-deethylated intermediates by spectrophotometry and HPLC provided with a diode array detector (C18 reverse phase column, mobile phase water (H<sub>2</sub>SO<sub>4</sub> 5mM)/methanol H<sub>2</sub>O:CH<sub>3</sub>OH = 35:65 v/v, flow rate of 0.8 mL/min, injection volume 50 ml). Aliquots of ca. 2 mL were removed periodically during the experiments and filtered (0.45 mm membrane filter) before measurement. Total organic carbon was followed also by means of a TOC analyzer (Shimadzu TOC VCPH).

The stability of the carbon phase in the composites during the photodegradation reaction was confirmed by characterizing aqueous dispersions of the composites exposed to 2 hours of irradiation in the absence of RhB, with no evidences of changes in the composition or the structure of the carbon component detected by XRD and XPS analysis (Table S1, Figure S4).



### 3. Results and discussion

The choice of the nanoporous carbons selected in this work for the preparation of the semiconductor/carbon photocatalysts was based on our previous studies reporting their intrinsic photochemical activity towards phenol photooxidation and their ability to generate radicals when exposed to UV light [14-18]. We herein describe their use as additives to BWO and discuss the effect on the catalytic performance of hybrid BWO/carbon composites under visible light for the degradation of a dye.

#### *3.1 Structural and textural characterization of the materials*

A detailed characterization of the synthesized composites and the as-received carbon materials was carried out before the photocatalytic runs. Figure 2 shows the XRD patterns of the photocatalysts; the diffraction patterns of  $\text{Bi}_2\text{WO}_6$  were well indexed to the russellite phase (JCPDS 39-0256, orthorhombic phase), constituted of a layered structure containing  $\text{WO}_6$  octahedra and  $(\text{Bi}_2\text{O}_2)^{2+}$  layers and  $\text{H}_2\text{O}$  molecules [23]. For the composites of the HS series, no evidences of diffraction peaks corresponding to  $\text{Bi}_2\text{O}_3$  or  $\text{WO}_3$  were observed, indicating the complete hydrolysis and assembly of the BWO precursors when the carbon component was present in the reaction medium. No other reflections associated to carbon phases (either amorphous or ordered) were seen in any of the XRD patterns of the composites. This is somehow expected due to the low amount of carbon additive (ca. 2wt.%) used in the preparation of the composites and their high dispersion in samples. However, the carbon additives themselves presented very different patterns pointing out the differences in their structural order (following the sequence: CNT>>> CL>CS, see Figure S3).

The line widths of the diffraction peaks were broad in all the samples, indicating small crystalline domain sizes. Crystallite size values obtained from the Scherrer's equation applied to the 131 plane (Table 1) were  $\sim 10$  and  $9$  nm for pristine calcined and non-calcined  $\text{Bi}_2\text{WO}_6$ ,

respectively, and are in agreement with previous studies [4-7,12,23]. As expected, the crystallinity was barely modified for the composites prepared by physical mixture (Table 1). On the other hand, slight changes are visible for the series HS, with values ranging between 8.1 and 8.9 nm indicating a distortion of the lattice of  $\text{Bi}_2\text{WO}_6$  when the synthesis of the semiconductor is carried out in the presence of the carbon additive. This effect was more remarkable for sample BWO/CS, prepared using carbon spheres from polysaccharides as an additive. Interestingly, similar results have been reported for carbon/BWO composites prepared using glucose as carbon precursor and showing much higher carbon contents [24].

Concerning morphology, bismuth tungstate nanostructures are highly dependent on the synthesis conditions (ca. solubility of the precursors, solution pH, surfactants as modifiers, temperature profile, time) [25], and many different shapes and topologies (nanorods, lamellar, octahedral, nanocages) have been reported. SEM images in Figure 3 showed that in our experimental conditions  $\text{Bi}_2\text{WO}_6$  consists mainly of flower-like shaped nanoparticles, with particle sizes ranging from 3-8 microns. Comparatively, the calcination of the semiconductor (PM vs HS) did not modify either the particle size or the shape of the particles (Figure 3). When the synthesis was carried out in the presence of the carbon additives (series HS), the 3D flower-like morphology was well-preserved, although the particle size was reduced (ca. 1-3 micron). This shows that the presence of the carbon does not affect the crystal growth rate of  $\text{Bi}_2\text{WO}_6$  and the aggregation of the clusters during the hydrothermal treatment, as opposed to other studies reporting self-assembling of the BWO particles (nanoplate and sheet-shaped like morphologies) due to the incorporation of the carbon phase [12,13]. We attribute this to the differences in the morphology of BWO and the carbon content, and to the fact that the average particle size of all carbon additives was smaller than that of BWO nanoparticles (Figures 3 and S5). The homogeneous dispersion of the additives within the matrix of the semiconductor in the HS series was confirmed by SEM images. Only in the case of BWO/CNT the SEM

micrographs allowed to distinguish bundles of carbon nanotubes between the sheets of the flower-like nanoparticles of the semiconductor (Figure 3).

The main textural parameters of the samples compiled in Table 1 show important textural differences between them. Data corresponding to the carbon materials used as additives is also included for clarity. All the composites displayed type II adsorption isotherms (Figure S6) characteristic of materials with a poor porous development. Only in the case of BWO/CL the isotherms present a somewhat microporous character, inherited from the large porosity of carbon CL. The increase in the gas uptake at relative pressures above 0.8 observed for all the samples is typically associated to either interparticle condensation (in the case of nanosized particles and/or bundles of carbon nanotubes), or to the presence of intraparticle mesoporosity. Given the relatively large particle size of the catalysts (Figure 3), interparticle condensation has been discarded, and the hysteresis loop is attributed to the condensation in the voids of the petals of the flower-like particles.

The main textural parameters (surface area and pore volume) of the composites prepared by physical mixture followed the expected trend as the experimental values match the stoichiometric calculations (theoretical) considering the loading of the carbon and the porosity of both precursors. This is reasonable considering that both -surface area and pore volume- are extensive magnitudes. In contrast, surface areas and micropore volumes of the samples prepared by the one-pot procedure were slightly larger than those of the PM series (Table 1). This suggests that the incorporation of the carbon particles inside the layered structure of  $\text{WO}_6$  octahedra and  $(\text{Bi}_2\text{O}_2)^{2+}$  units gives rise to intraparticle voids seen in the nitrogen adsorption data (despite no changes were observed in the crystallinity).

### *3.2. Acid/base characterization of the catalysts*

Additional differences were observed in the acidic/basic nature of the catalysts, as determined by the surface pH (Table 1) and the proton binding curves (Figure 4). First of all, the higher acidic character of the non calcined bare semiconductor, based on the surface pH values should be pointed out. This effect cannot be attributed to the excess of acetic acid used in the synthesis as all the samples were extensively washed with distilled water (ca. 300 mL), thus is linked to hydroxyl groups on the surface of BWO that would be removed during the calcination step. The effect of the nature of the carbon additives is also noticed in the composites, as those based on acidic CS and CL carbons display a lower pH than the sample prepared using the CNT -of basic nature- as additive (Table 1). Besides, the composites prepared by the one-pot route are comparatively more hydrophilic than those prepared by physical mixture, regardless the carbon additive.

Further insight on the acidic/basic properties of the catalysts was obtained by potentiometric titration, a very useful technique for determining the status of the catalyst's surface in aqueous solution [20,26]. Figure 4 shows the proton binding curves of the catalysts, compared to those of the individual components. Both BWO samples (either calcined or not) displayed a similar pattern with  $Q(H^+)$  values close to zero up to pH below 8, indicating a zero net and absolute charge due to low adsorption and release of protons from the electrolyte. The slight deviation to negative values of  $Q(H^+)$  at pH above 8 indicate proton release attributed to distinct hydroxyl and/or oxo groups in several configurations (monodentate, bidentate) [20]. For the composites, it is worth noting that those prepared by physical mixture of the components (series PM) are more positively charged than those of the HS series, in agreement with the less acidic surface pH. Also, the negatively charged surface of the HS series at pH 4-6 indicates the presence of Bronsted acid sites in these catalysts.

The surface composition and chemical states of the catalysts was further investigated by XPS (Table 2 and Figure S7). The spectra of bare BWO displayed the characteristic spin-orbit split

of Bi 4f<sub>5/2</sub> and Bi 4f<sub>7/2</sub> signals at 165.3 and 159.9 eV assigned to trivalent bismuth, along with the doublet of tungsten components in W<sup>6+</sup> oxidation state at 38.3 and 36.3 eV. These profiles are consistent with those reported for BWO in the literature [21, 27, 28].

For the composites, the bands corresponding to Bi and W became somewhat broader, particularly for BWO-CS and BWO-CL; we attribute this to a poor surface charging of both samples due to the presence of the poor conductive carbon additive, as opposed to BWO-CNT. Interestingly, the binding energies for Bi and W in the composites shifted towards lower values, indicating a subtle change in the chemical environment of these elements upon the incorporation of the carbon additives. The downward shift indicates a reduction of the local charge in the metallic atoms, suggesting the formation of a carbon-semiconductor heterojunction. This was not observed in the PM series, confirming the enhanced contact of both components during the one-pot synthesis (as opposed to physical mixture).

The analysis of the O1s core spectra signals was not performed due to the high density of O-groups in the carbon additives, that lead to the overlapping of the peaks assigned to metal-oxide and metal-OH environments (at 530.9 and 531.9 eV for Bi and W) with those assigned to C=O and C-O moieties (in the range of 531-532 and 532.5-533.5 eV) in the carbons.

### 3.3. *Optical properties of the catalysts*

The optical properties of the samples were also explored by UV-Vis diffuse reflectance spectroscopy (Figure 5). Commercial TiO<sub>2</sub> (P25, Evonik) with anatase/rutile structure is also shown as reference. The spectrum of BWO presented the characteristic absorption sharp edge above 400 nm (the onset wavelength estimated at the intersection of the extrapolated linear segments of the absorption edge at maximum reflectance and the photon energy axis was ca. 385 nm; see example in Figure S8) of Bi-containing oxides [28] due to the transitions from the O2p and Bi6s hybrid orbitals to the W5d and Bi6p orbitals. The calcination of the bare semiconductor did not change its optical response or band gap.

At converse, the incorporation of the carbon additives modified the optical properties of BWO despite the low amount used. Regardless the synthesis route, all the BWO/C composites showed a pronounced increase in the absorption between 450-800 nm (visible range). This can be attributed to either the presence of photo-sensitive functional groups on the carbon matrix [29] or to the reduced reflectivity introduced by black samples [30,31]. Indeed, the light absorption of the BWO/C composites above 450 nm followed the order: CNT > CL > CS, which matches the thermal history of the carbon materials (CNT were synthesized at 700 °C, CL at 650°C and CS at 180°C). Thus the more evolved carbon has the higher light absorption in the visible range. This was also observed in the color of the composites (Figure 1), darker for CNT than CL or CS; this effect was more remarkable for HS, but can be also clearly observed in the PM series.

Interestingly, the differences detected in the color of the composites for the PM and HS series are in agreement with the diffuse reflectance spectra. Beside the above-mentioned reduced reflectivity of dark samples, the sharp absorption threshold around 400 nm characteristic of BWO is well defined for all the composites prepared by physical mixture of the components, as well as for sample BWO/CNT HS (Figure 5). In contrast, samples BWO/CS HS and BWO/CL HS show a distinct curvature in the adsorption profile above 445 nm (see arrow in Figure 5). The smooth increasing slope between 445 nm and up to maximum reflectance of both samples, contrasts with the sharp absorption cut-off of BWO, TiO<sub>2</sub> and BWO/CNT samples. A somewhat similar trend is observed for BWO/CS PM although the curvature appears at higher wavelength, above 550 nm. Similar results on the visible light harvesting properties of carbon materials prepared from renewable precursors have been reported in the literature [29]. Furthermore, it should be noted that these three materials presented a lighter color (Figure 1). We attribute this behavior to the highly functionalized surface of CS and CL

carbons (Table 1 and Figure 4), hence suggesting the presence of photo-sensitive functional groups.

These changes in the surface chemistry would induce the modifications seen in the diffuse reflectance spectra. We have found a similar pattern for TiO<sub>2</sub>/carbon and WO<sub>3</sub>/carbon composites (data not shown) when the carbon additive is highly functionalized, confirming this premise [32,33]. This behavior is expected to lead to modifications of the fundamental process of electron/hole pairs photogeneration and/or recombination upon irradiation of the composites.

Band-gap energies were calculated by plotting  $(F(R_{\infty}) \cdot hv)^{1/n}$  against  $hv$  (best fitting was obtained for  $n = 1/2$  characteristic of direct allowed transitions), and the corresponding values are shown in Table 1. Values for bare BWO and the composites were close to those reported in the literature for other carbon/Bi<sub>2</sub>WO<sub>6</sub> materials [12,13,24,28]. It should be noted that the band gap values obtained for the HS series are close to those of bare BWO and similar between them, with a negligible effect of the carbon component. In contrast, for the PM series, the band gap is reduced compared to BWO, being the effect more remarkable for the composite incorporating carbon nanotubes (ca. the darkest carbon additive).

### *3.4 Photocatalytic experiments*

#### *3.2.1. Dark adsorption*

Given the porosity of the BWO/C catalysts (Table 1) inherited by the carbon additives, we initially investigated the uptake of RhB on the carbon materials under dark conditions. This would enable to discriminate between the removal of the pollutant due to adsorption and due to the photooxidation reaction, as both take place simultaneously in porous catalysts.

Adsorption capacities of 110, 370 and 155 mg RhB adsorbed/g were obtained for CS, CL and CNT, respectively. To understand these large differences we must have in mind that the adsorption of ionic dyes as RhB on a porous material depends not only on the porosity of the adsorbent but also on the specific interactions at the adsorbent surface involving the different charged forms. RhB is an amphoteric dye with a permanent positive charge (diethylamino group) and a negative charge upon dissociation of the carboxylic moiety. Under our experimental conditions RhB is in the zwitterionic form in the aqueous solution, with predominance of positive charges. Thus, the uptake of RhB is controlled by the electrostatic interactions between the catalyst surface and the charges of the dye [28,34]. The electrostatic interactions at the solution/solid interfaces also control the preferential orientation of the adsorbed RhB molecules [34,35]: on negative surfaces, RhB is adsorbed by the diethylamino group (positively charged), whereas for positively charged surfaces the preferred adsorption mode is through the carboxylic group of RhB. Knowledge on the adsorption modes of the pollutant on the surface of photocatalysts is of paramount importance as it may determine its photocatalytic degradation pathway [33,36].

Considering the different RhB adsorption capacities of the carbon additives, the photocatalytic runs were carried out on catalysts previously exposed to RhB under darkness, so as to allow the adsorption of the pollutant at equilibrium conditions. Hence the initial concentration of RhB in the solution was adjusted for each BWO/carbon composite so as to obtain the same value at the beginning of the illumination period (after adsorption in the dark).

### *3.2.2. Rhodamine B conversion*

Figure 6 and Table 3 show the effect of the carbon additive on the photocatalytic activity of  $\text{Bi}_2\text{WO}_6$  for the photodegradation of RhB under visible light irradiation in terms of pollutant conversion and mineralization (evaluated by the TOC values) from the solution. First of all, it



should be pointed out that degradation of RhB by direct photolysis was very low under our irradiation (Figure 6), with an overall mineralization below 5 % (Table 3). Also, it is observed that the calcination of the semiconductor has a small effect on the conversion of RhB (Figure 6, inset); conversions at short times are similar, but the calcined sample showed a less steep profile after 60 min suggesting that the degradation is gradually slowed down after some time, likely as a result of the simultaneous degradation of the intermediates along with that of RhB itself. This contrasts with the similar morphology and crystallinity of both samples (Table 1), and points out that the slight differences in surface acidity and porosity are important in the photocatalytic properties of BWO [37-39].

Secondly, with the exception of BWO/CNT, the conversion of RhB was enhanced for the composites prepared by incorporation of the carbon additive before the hydrothermal synthesis of the semiconductor (series HS). The superior photocatalytic activity of BWO/carbon composites with nominal carbon contents between 0.5 and 25 wt.% has been reported for other additives (e.g., activated carbons, graphene or glucose-derived carbons) [12,13,24]. In our case the effect was very pronounced for BWO/CS, particularly within the first 60 min of illumination leading to almost full RhB conversion. Nonetheless, the overall conversion and mineralization after 2 hours of irradiation was quite similar for all the samples. It is interesting to note that BWO/CNT composite showed lower catalytic activity than bare BWO, also displaying the lowest mineralization extent (Table 3). This shows that despite the high electron mobility of carbon nanotubes (that would anticipate a lower recombination of the photogenerated exciton), their use as additives to semiconductors does not grant a superior photocatalytic performance of the resulting composites. In our case, we believe this is attributed to the strong light absorption of the nanotubes, as revealed by the poor optical features of the composite shown in Figure 5.

Comparatively, a poor photocatalytic activity was obtained for the composites prepared by physical mixture of the precursor's powders, regardless the carbon material. Conversions below 70 % were obtained for all the samples, far below those of BWO, and the effect is noticed at short illumination periods. This contrasts with the wide number of studies (including our own) on other semiconductor/carbon composites prepared by physical mixture where the effect of the carbon additive is quite the opposite [8-11]. We attribute this to the large particle size of BWO (Figure 3) compared to usually nanometric size of other semiconductors, that would limit the contact between the carbon particles and the semiconductor. All this points out the importance of the synthetic method followed to build an effective interface between the carbon and semiconductor particles and to achieve a superior photocatalytic performance with a given photocatalysts.

### *3.2.2. Intermediates speciation and/or degradation mechanism*

Regarding intermediates, the evolution of the N-deethylated compounds for the HS series of catalysts is shown in Figure 7. The concentration of poly-N-deethylated compounds (DER<DR~ER< EER<R) gradually increases with time for all the catalysts; the most N-deethylated intermediate is only detected after 60 min, showing that RhB photooxidation occurs via successive N-deethylation reactions rather than by direct chromophore cleavage [12]. The degradation mechanism follows a similar pattern for the BWO/carbon composites, indicating that the effect of the carbon additive is linked to the kinetics of the photooxidation reaction rather than to a mechanistic change. Indeed, Figure 7 shows that the rate of the successive N-deethylation reactions is enhanced for BWO/CS and BWO/CL, with almost no intermediates detected after 70-80 min, indicating a high conversion involving the total degradation of RhB (Table 3). At least twice longer times are needed to achieve similar results for BWO and BWO/CNT.

These findings are in good agreement with the preferred adsorption mode of RhB on the surface of the catalysts, as discussed above. Under our experimental conditions, the surface of the composites of the HS series is negatively charged (Figure 4b), thus RhB is preferentially adsorbed by the diethylamino group (positively charged) [34,40]. Consequently, the degradation of RhB is favored by the attack of the active oxygen species generated nearside the adsorption sites to the auxochromic  $C_2H_5$  groups of RhB, inducing the deethylation of the alkylamine moiety. This is supported by the marked gradual hypsochromic shift in the UV-vis spectra of the aqueous dye solution (an example of the progress in the photocatalytic degradation of RhB by a catalyst of the HS series is presented in Figure S9), that is associated to the stepwise formation of N-deethylated degradation subproducts [34,40]. The strict requirements needed for the N-deethylation process (i.e., formation of the excited state of the dye and transfer of electrons from the dye to the conduction band of the semiconductor) point out the good chemical contact between the catalyst surface and the dye, provided by the incorporation of the acidic carbon additives.

Additionally, the concentration of RhB faded completely after 60 min for BWO/CS and BWO/CL (HS series); this evidences that N-deethylation is not the only mechanism, as the reaction would then terminate with the formation of the fully N-deethylated intermediate. Based on the RhB conversion and high mineralization values (Table 3), degradation via the chromophore cleavage also occurs simultaneously. This seems plausible as both mechanisms are independent and can proceed side by side (Figure 8).

In the case of positively charged catalyst's surfaces (sample CNT/BWO HS and the catalysts of the PM series), the preferred adsorption mode of RhB is through the negative charge of the carboxylic moiety; as the relative abundance of negative charges on RhB aqueous solution is low, the interactions with the catalyst surface are lesser (weaker). This partially suppresses the degradation via the deethylation process (although still present as seen in Figures 7 and S7),

accounting for the lower conversions of these composites. Similar results have been reported for TiO<sub>2</sub> and TiO<sub>2</sub>/SiO<sub>2</sub> surfaces, with an accelerated degradation rate for negatively charged surfaces due to successive N-deethylation reactions [34,40].

To further analyze the effect of the nature of the carbon additive we must consider the differences between the catalysts in terms of porosity, composition and acidic nature. First of all, it should be noticed that both RhB and BWO absorb light during the photocatalytic runs [37]. As shown in Figure 5, BWO absorbs light at  $\lambda < 400$  nm, whereas RhB absorbs in the range 460-600 nm (Figure S9) owing to intramolecular  $\pi-\pi^*$  transitions leading to the formation of an excited state of the dye. Consequently, the photodegradation of RhB can proceed via two different mechanisms: photocatalysis or photosensitization (Figure 8).

As seen in Figure 6, direct degradation of RhB upon illumination is very low (ca. below 5 %), indicating that degradation via the photosensitized process does not occur in the absence of a catalyst. In the presence of BWO, the excited state of RhB is firstly formed and the photoelectrons are injected into the conduction band of Bi<sub>2</sub>WO<sub>6</sub>, where they can be captured by the dissolved oxygen in the solution (preventing the recombination) and leaving holes in the valence band capable of direct oxidation. The succeeding reactions involving oxygen radical species and/or direct hole oxidation would lead to the mineralization of the dye, as seen in Table 3 [29,41]. The photosensitized process would only occur if the interaction between RhB and the surface of the catalysts is strong enough to have an efficient injection of electrons from the dye to the surface of the semiconductor [42-44]. Simultaneously, the photocatalytic process initiated by the light-excitation of Bi<sub>2</sub>WO<sub>6</sub> also takes place, leading to RhB degradation; in fact, the light-excited semiconductor reaction is usually a much faster reaction than the photosensitized degradation.

In the case of BWO/carbon composites of the HS series the photosensitized mechanism would be expected due to the chemical and textural characteristics of the catalysts provided by the

carbon additives. The high adsorption capacity of the carbon materials and the acidic nature of the composites favor strong interactions between RhB and the photocatalyst surface in acidic materials, which is crucial for an efficient photosensitized process [37]. This would explain why the photooxidation yield obtained for BWO/CNT is similar to that of bare BWO; even though the adsorption capacity on the CNT is not negligible, the interaction between RhB and the photocatalyst surface is weak due to the basic nature of the carbon additive (Table 1 and Figure 4). Hence, the degradation is expected to occur only via the photocatalytic process. For acidic catalysts as BWO, BWO/CS and BWO/CL, the interaction between the RhB and the acidic sites seems strong enough to promote the photosensitized process, in addition to the photocatalytic one. Furthermore, according to literature, the photosensitized pathway leads to the N-deethylation of RhB, which commensurate with the evolution in intermediates seen in Figure 7, and confirms the interaction of the catalysts acid sites through the diethylamino group.

Also, it should be mentioned that the carbon additives herein used showed a non-negligible intrinsic photoactivity under UV-Vis illumination due to the ability to photogenerate oxygen radical species [14-16]. The superior activity of the hybrid BWO/carbon composites studied could also be partly boosted by the carbon-photon interactions, as they are capable of propagate through the material and generate oxygen radical species nearby the adsorbed molecules [14,15]. Thus, similarly to the role of RhB, the carbon additive would act as either a photosensitizer injecting electrons to the semiconductor, or as an electron acceptor (Figure 8) contributing to enhance the charge separation (due to the delocalization of the electrons in the  $\pi$ -electron density of the graphenic layers) in a process analogous to that reported for deposited noble metals [45]. The charge separation ability of the carbon additives should be related to their structural and electronic properties, and hence would be favored for the composites incorporating CNT (electrical conductivity values of ca. 13, 0.22 and 0.01

S/cm for CNT, CL and CS, respectively). However, this trend does not explain either the superior activity of BWO/CS and BWO/CL compared to BWO/CNT, or that of HS over PM series, indicating that other factors need to be considered. We attribute the low performance of the composites prepared by physical mixture to the shielding effect of the carbon matrix (Figure 1 shows the darker color of the PM composites) incorporated outside the semiconductor particles. For the catalysts prepared by the one-pot route, the carbon particles would be embedded in the core of the semiconductor (Figure 3), reducing the shielding effect while improving dispersion and contact between both components.

Summarizing, all this points out that the impact of introducing carbon additives in the formulation of semiconductors goes beyond the increased surface area and electron mobility reported in the literature [8,9,29,30]. The carbon material is capable of boosting the surface acidity of the hybrid photocatalyst, thus enhancing the photodegradation of RhB under visible light via a coupled mechanism. The incorporation of only 2 wt.% of CL and CS acidic carbons as additives renders much faster photodegradation kinetics. This is most remarkable bearing in mind that both are amorphous carbons obtained from low-cost precursors, compared to nanostructured and high-cost carbon nanotubes.

#### **4. Conclusions**

We have investigated the influence of the properties of carbon additives on the catalytic performance of  $\text{Bi}_2\text{WO}_6$  towards the photooxidation of RhB from solution under visible irradiation. Besides the textural and chemical characteristics of the carbon, the synthetic route chosen to incorporate the additive is important to obtain an effective interface between the catalyst's components, and thus an enhanced photocatalytic performance.

The presence of a low nominal content of carbon additives does not modify significantly the hydrothermal synthesis of the semiconductor: yield, particle morphology or crystallinity

remained the same, with just a small shrinkage of the particle sizes. In contrast, noticeable changes are observed in the optical properties of the composites, with an increase in the absorption in the visible range. This effect seems to be linked to the degree of evolution of the carbon additive incorporated.

Regarding the photocatalytic experiments, the degradation of RhB was much faster for those composites prepared through a one-step hydrothermal synthesis than for the ones obtained by physical mixture, where the shielding effect of the carbon matrix was more pronounced. Moreover, the photocatalytic performance of the HT series was higher than for the bare BWO, with the exception of the BWO/CNT composite. The superior photoactivity of the hybrid BWO/CS HT and BWO/CL HT is likely attributed to the formation of carbon-semiconductor heterojunctions and to their acidic nature, favoring the degradation of the pollutant by a photosensitized process, in addition to the photocatalytic one. Also, the superior activity of the corresponding hybrid composites could also be partially due to the carbon-photon interactions leading to the formation of O-radicals.

## **ACKNOWLEDGMENTS**

The authors thank the financial support of MINECO (grants CTM2011/23378 and CTQ2011/26617) and PCTI Asturias (Fondos Feder 2007-2013, grant PC10-002). RJC thanks PCTI Asturias for her Severo Ochoa fellowship.

## **References**

- [1] N. Serpone, E. Pelizzetti, *Photocatalysis: fundamental and applications*; Wiley Interscience, New York, 1989.

- [2] T. Oppelander, Photochemical purification of water and air: advanced oxidation processes (AOPs): Principles, reaction mechanisms, reactor concepts; Wiley-VHC, Weinheim, 2003.
- [3] M.A. Henderson, Surf. Sci. Reports 66 (2011) 185-297.
- [4] G. Colón, S. Murcia-López, M.C. Hidalgo, J.A. Navío, Chem. Commun 46 (2010) 4809-4811.
- [5] J.G. Yu, J.F. Xiong, B. Cheng, Y. Yu, J.B. Wang, J. Solid State Chem 178 (2005) 1968-1972.
- [6] C. Zhang, Y.F. Zhu, Chem. Mater. 17 (2005) 3537-3545.
- [7] J.W. Tang, Z.G. Zou, J. Ye, Catal. Lett. 92 (2004) 53-56.
- [8] R. Leary, A. Westwood, Carbon 49 (2011) 741-72.
- [9] J.L. Faria, W. Wang, Carbon materials in photocatalysis, in: P. Serp, J.L. Figueiredo (Eds.), Carbon materials for catalysis, John Wiley & Sons, New York, 2009, pp. 481-506.
- [10] C.O. Ania, L.F. Velasco, T. Valdes-Solis, Photochemical response of carbon materials. in: J.M.D. Tascon (Ed.), Novel Carbon Adsorbents, Elsevier, London, 2012, pp. 521-547.
- [11] J. Araña, J.M. Doña-Rodríguez, E. Tello Rendón, C. Garriga i Cabo, O. González-Díaz, J.A. Herrera-Melián, J. Pérez-Peña, G. Colón, J.A. Navío, Appl. Catal. B: Environ. 44 (2003) 161-172.
- [12] S. Murcia-López, M.C. Hidalgo, J.A. Navío, Appl. Catal. A: Gen. 466 (2013) 51-59.
- [13] Y.Y. Li, J.P. Liu, X.T. Huang, J.G. Yu, J. Chem. Soc. Dalton Trans. 39 (2010) 3420-3425.
- [14] L.F. Velasco, I.M. Fonseca, J.B. Parra, J.C. Lima, C.O. Ania, Carbon 50 (2012) 249-258.



- [15] L.F. Velasco, J.C. Lima, C.O. Ania, *Angew. Chem. Int. Ed.* 53 (2014) 4146-4148.
- [16] L.F. Velasco, V. Maurino, E. Laurenti, C.O. Ania, *Appl. Catal. A: Gen.* 453 (2013) 310-315.
- [17] L.F. Velasco, R.J. Carmona, J. Matos, C.O. Ania, *Carbon* 73 (2014) 206-2015.
- [18] L.F. Velasco, Ph.D. Thesis, University of Oviedo, 2012. Available at:  
[http://digital.csic.es/bitstream/10261/72354/1/Tesis\\_Leticia%20Fdez%20Velasco\\_2012.pdf](http://digital.csic.es/bitstream/10261/72354/1/Tesis_Leticia%20Fdez%20Velasco_2012.pdf)
- [19] J. Rouquerol, F. Rouquerol, P. Llewellyn, G. Maurin, K.S.W. Sing, *Adsorption by Powders and Porous Solids. Principles, Methodology and Applications*, second ed., Academic Press, Amsterdam, 2014.
- [20] J. Jagiello, T.J. Bandosz, J.A. Schwarz, *Carbon* 32 (1994) 1026.
- [21] J.F. Moulder, W.F. Stickle, P.E. Sobol, K.D. Bomben, *Standard Spectra for Identification and Interpretation of XPS data*, Perkin Elmer, Eden Prairie, MN, 1992.
- [22] H.K Kuhn, S.E. Braslavsky, R. Schmidt, *Pure App. Chem.* 76 (2004) 2105-2146.
- [23] C. Ng, A. Iwase, Y.H. Ng, R. Amal, *J. Phys. Chem. Lett.* 3 (2012) 913.
- [24] Y. Cui, L. Huiquan, H. Wenshan, F. Suhua, Z. Liangjun, *Powder Technol.* 247 (2013) 151-160.
- [25] L.W. Zhang, Y.F. Zhu, *Catal. Sci. Technol.* 2 (2012) 694.
- [26] C. Contescu, J. Jagiello, J.A. Schwarz, *Langmuir* 9 (1993) 1754-1765.
- [27] L. Yue, S. Wang, G. Shan, W. Wu, L. Qiang, L. Zhu, *Appl. Catal. B: Envir.* 176 (2015) 11-19.
- [28] H. Fu, C. Pan, W. Yao, Y. Zhu, *J. Phys. Chem. B* 190 (2005) 22432-22439.
- [29] J. Matos, A. García, L. Zhao, M.M. Titirici, *Appl. Catal. A: Gen.* 390 (2010) 175-182.
- [30] J. Araña, J.M. Doña-Rodríguez, E. Tello Rendón, C. Garriga i Cabo, C. González-Díaz, J.A. Herrera-Melián, J. Pérez-Peña, G. Colón, J.A. Navío, *Appl. Catal. B: Environ.* 44 (2003) 153-160.

- [31] L.F. Velasco, J.B. Parra, C.O. Ania, *Adsorpt. Sci. Technol.* 28 (2012) 727-738.
- [32] L.F. Velasco, M. Haro, J. Parmentier, R. Gadiou, C. Vix-Guterl, C.O. Ania., *J. Catalysts* 2013 (2013) Article ID 178512, 9 pages.
- [33] R. J. Carmona, L.F. Velasco, C.O. Ania, Carbon additives for an enhanced visible light activity of Bi/W/Ti based semiconductors, *Proceedings of the International Carbon Conference, Korea* (2014) 2 pag (OR-S10-173).
- [34] H. Gad, A.A. El-Sayed, *J. Hazard. Mater.* 168 (2009) 1070-1081.
- [35] I. Lopez-Arbeloa, P. Ruiz Ojeda, *Chem. Phys. Lett.* 87 (1982) 556-560.
- [36] F. Chen, J. Zhao, H. Hidaka, *Int. J. Photoenergy* 5 (2003) 209-217.
- [37] Y. Xu, C.H. Langford, *Langmuir* 17 (2001) 897.
- [38] G. Liu, T. Wu, J. Zhao, H. Hidaka, N. Serpone, *Environ. Sci. Technol.* 33 (1999) 2081-2087.
- [39] T. Saison, N. Chemin, C. Chaneac, O. Durupthy, V. Ruaux, L. Mariey, F. Mauge, P. Beaunier, J.P. Jolivet, *J. Phys. Chem. C* 115 (2011) 5657-5666.
- [40] O. Merka, V. Yarovyi, D.W. Bahnemann, M. Wark, *J. Phys. Chem. C* 115 (2011) 8014-8023.
- [41] P. Wang, M. Cheng, Z. Zhang, *J. Saudi. Chem. Soc.* 18 (2014) 308-316.
- [42] J.B. Asbury, E. Hao, Y. Wang, T. Lian, *J. Phys. Chem. B* 104 (2000) 11957-11964.
- [43] N.A. Anderson, X. Ai, D. Chen, D.L. Mohler, T. Lian, *J. Phys. Chem. B* 107 (2003) 14231-14239.
- [44] E. Galoppini, *Coord. Chem. Rev* 248 (2004) 1283-1297.
- [45] W. Wang, P. Serp, P. Kalck, J.L. Faria, *J. Mol. Catal. A: Chem* 235 (2005) 194-199.

## Figures Captions

**Figure 1.** Images of hybrid catalysts prepared by incorporation of the carbon additive before the hydrothermal synthesis of the semiconductor (series HS) or by physical mixture of the carbon and  $\text{Bi}_2\text{WO}_6$  powders (series PM).

**Figure 2.** X-ray diffraction patterns of the prepared catalysts. Diffractograms have been shifted for clarity.

**Figure 3.** SEM images of the catalysts.

**Figure 4.** Proton binding curves of the carbon materials, bare semiconductors and hybrid composites.

**Figure 5.** Diffuse Reflectance spectra of the synthesized catalysts.

**Figure 6.** Rhodamine B conversion upon visible light irradiation of the catalysts prepared by incorporation of the carbon additives before the hydrothermal step (A) and by physical mixture of the powders (B). (inset) effect of the calcination treatment on the bare semiconductor.

**Figure 7.** Evolution of RhB intermediates upon irradiation of the studied catalysts with visible light.

**Figure 8.** Schematic representation of the different degradation routes of RhB in the presence of BWO and BWO/carbon photocatalysts.

**Table Captions**

**Table 1.** Main structural, textural and physicochemical parameters of the studied materials obtained from gas adsorption data, XRD and elemental analysis.

**Table 2** Surface concentration of elements (in at. % from XPS analysis) in the catalysts prepared through the one-pot synthesis (HS series), and chemical shift of the Bi 4f core level versus bare BWO.

**Table 3.** TOC values upon 2 hours of irradiation of the studied catalysts.



**Figure 1.** Images of hybrid catalysts prepared by incorporation of the carbon additive before the hydrothermal synthesis of the semiconductor (series HS) or by physical mixture of the carbon and  $\text{Bi}_2\text{WO}_6$  powders (series PM).

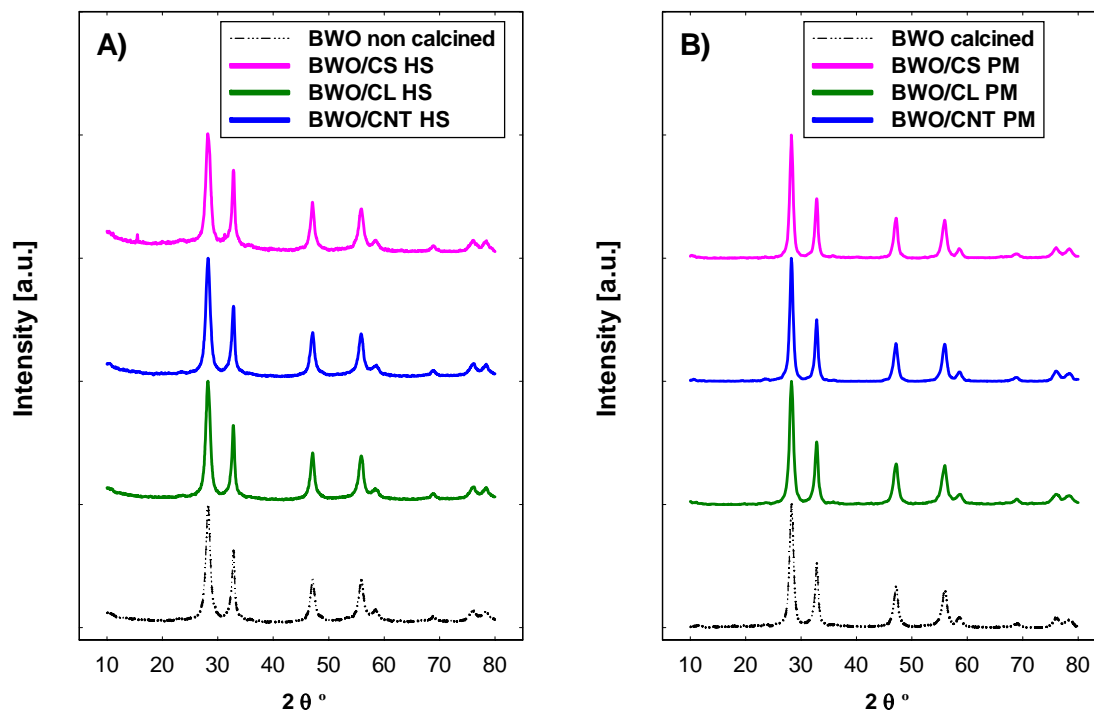


**Figure 2.** X-ray diffraction patterns of the prepared catalysts. Diffractograms have been shifted for clarity.

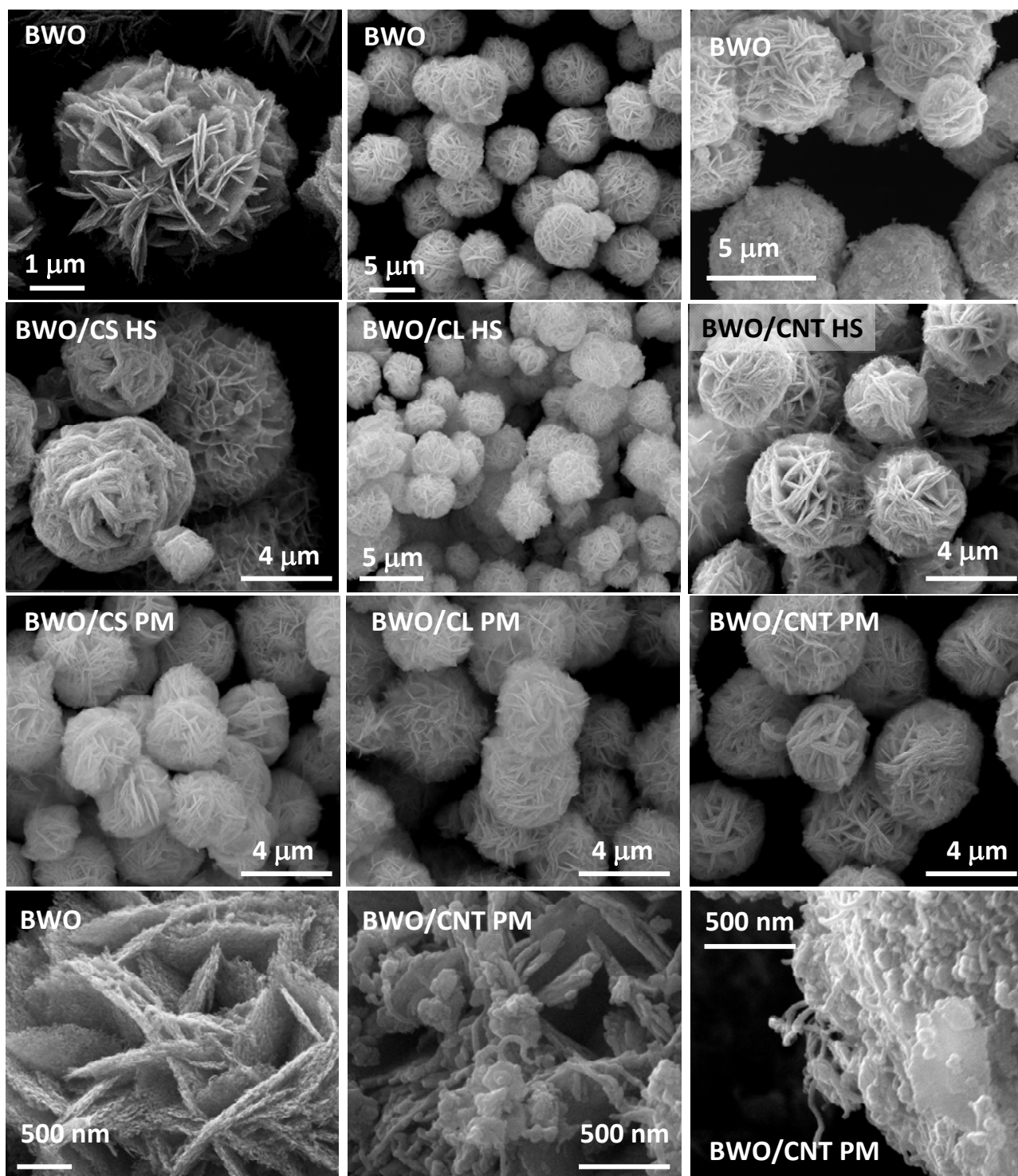


**Figure 3.** SEM images of the catalysts.

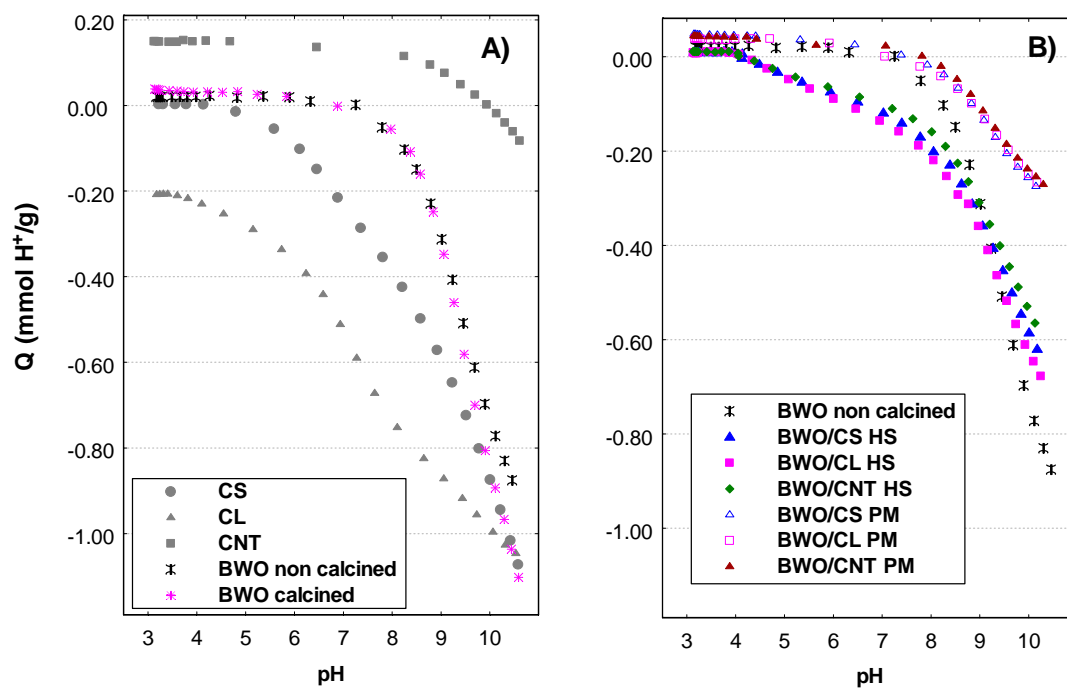


**Figure 4.** Proton binding curves of the carbon materials, bare semiconductors and hybrid composites.



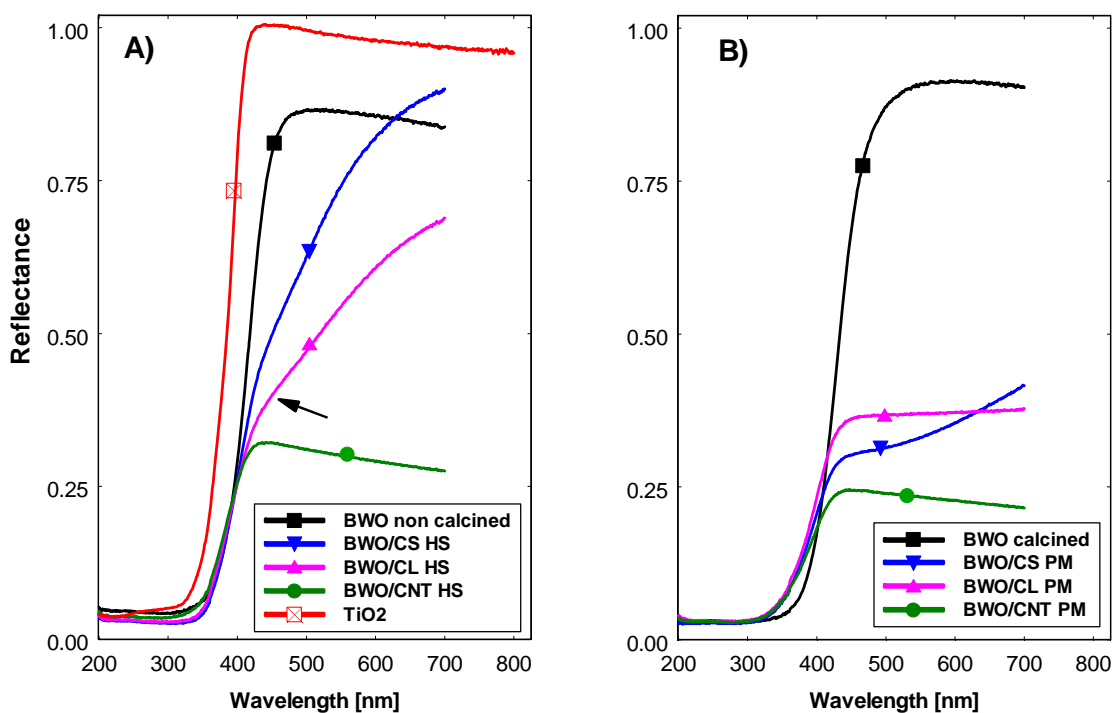


**Figure 5.** Diffuse Reflectance spectra of the synthesized catalysts.

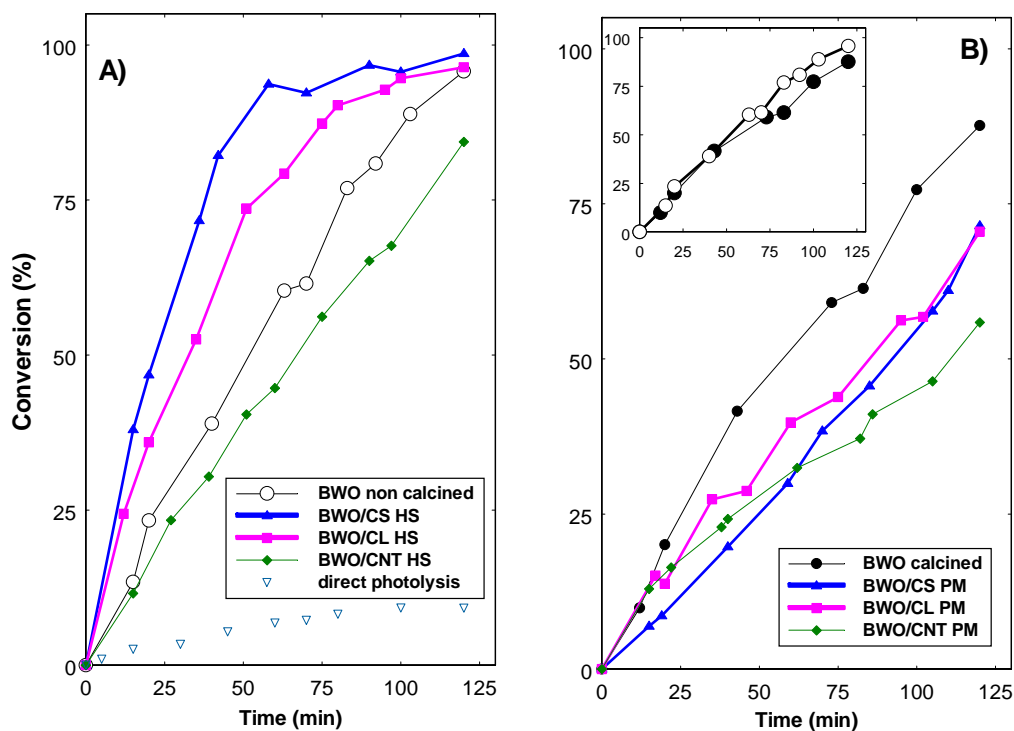


**Figure 6.** Rhodamine B conversion upon visible light irradiation of the catalysts prepared by incorporation of the carbon additives before the hydrothermal step (A) and by physical mixture of the powders (B). (inset) effect of the calcination treatment on the bare semiconductor.

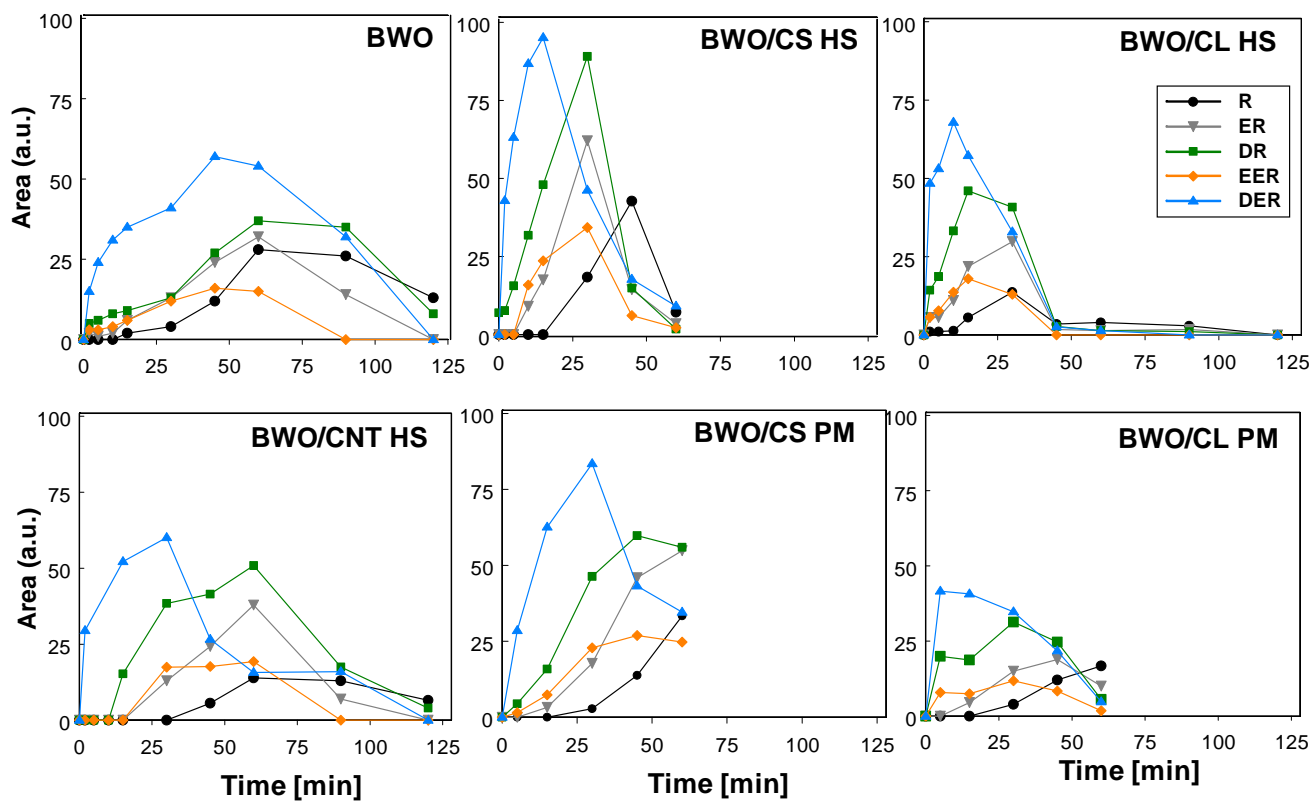


**Figure 7.** Evolution of RhB intermediates upon irradiation of the studied catalysts with visible light.

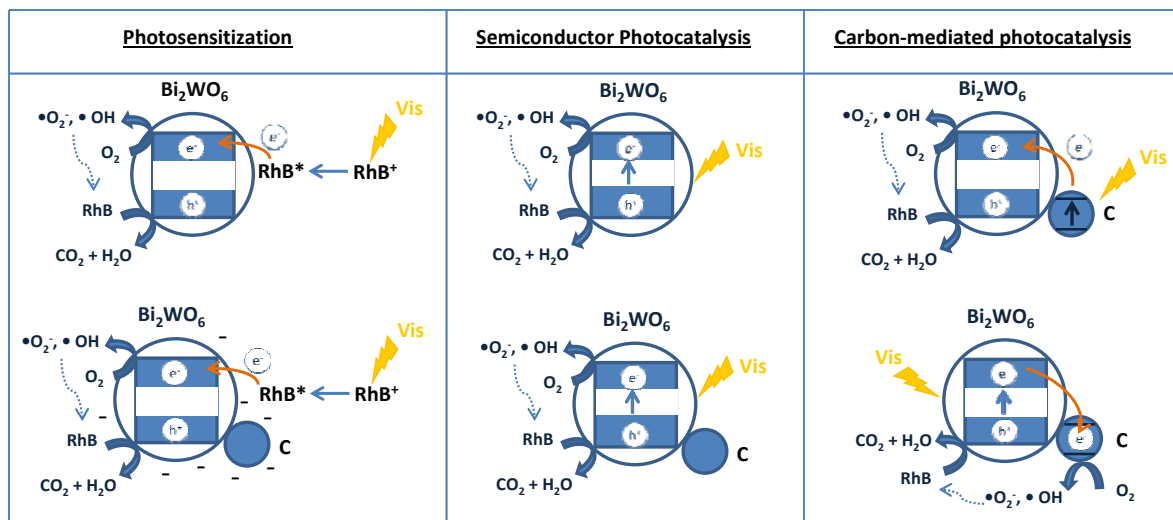


**Figure 8.** Schematic representation of the different degradation routes of RhB in the presence of BWO and BWO/carbon photocatalysts.

**Table 1.** Main structural, textural and physicochemical parameters of the studied materials obtained from gas adsorption data, XRD and elemental analysis.

	$S_{\text{BET}}$ ( $\text{m}^2 \text{g}^{-1}$ )	$V_{\text{total}}^1$ ( $\text{cm}^3 \text{g}^{-1}$ )	$V_{\text{micro}}^2$ ( $\text{cm}^3 \text{g}^{-1}$ )	surface pH	$d^3$ (nm)	Band gap (eV)
<b>BWO/CS PM</b>	28	0.104	0.008	5.5	10.6	2.68
<b>BWO/CL PM</b>	39	0.089	0.013	4.8	9.7	2.76
<b>BWO/CNT PM</b>	33	0.131	0.011	5.9	10.5	2.47
<b>BWO/CS HS</b>	41	0.106	0.013	4.6	8.3	2.84
<b>BWO/CL HS</b>	43	0.123	0.014	4.5	8.8	2.86
<b>BWO/CNT HS</b>	45	0.131	0.014	4.6	8.9	2.86
<b>BWO calc</b>	28	0.086	0.007	5.7	9.9	2.90
<b>BWO non calc</b>	33	0.08	0.01	4.9	9.1	2.89
<b>CS</b>	8	0.014	0.001	4.3	--	--
<b>CL</b>	1280	1.03	0.27	3.6	--	--
<b>CNT</b>	298	2.09	0.20	8.6	--	--

<sup>1</sup> evaluated at  $p/p^0 = 0.9$   
<sup>2</sup> evaluated by DR method  
<sup>3</sup> crystallite size evaluated from XRD data

**Table 2** Surface concentration of elements (in at. % from XPS analysis) in the catalysts prepared through the one-pot synthesis (HS series) and chemical shift of the Bi 4f core level versus bare BWO.

	<b>BWO</b>	<b>BWO/CS HS</b>	<b>BWO/CL HS</b>	<b>BWO/CNT HS</b>
<b>Bi (at. %)</b>	21.4	21.0	20.8	21.24
<b>W (at. %)</b>	10.1	7.2	7.0	7.1
<b>C (at. %)</b>	1.6	38.1	44.9	27.6
<b>O (at. %)</b>	66.9	33.7	27.3	44.9
<b>Chemical shift Bi 4f (eV)</b>	--	<b>0.1</b>	<b>0.3</b>	<b>0.2</b>
<b>Position Bi 4f (eV)</b>	<b>159.9</b>	<b>159.8</b>	<b>159.6</b>	<b>159.7</b>

**Table 3.** TOC values upon 2 hours of irradiation of the studied catalysts.

	<b>Initial TOC mg C/L</b>	<b>Final TOC mg C/L</b>	<b>Mineralization (%) [1-(Final TOC/InitialTOC)]</b>
<b>RhB direct photolysis</b>	6.8	6.5	<b>4.4</b>
<b>BWO non calcined</b>	6.8	0.3	<b>95.6</b>
<b>BWO/CS HS</b>	6.7	0.1	<b>98.4</b>
<b>BWO/CL HS</b>	8.2	0.3	<b>96.4</b>
<b>BWO/CNT HS</b>	6.2	1	<b>83.9</b>
<b>BWO calcined</b>	7.0	1.2	<b>83.6</b>
<b>BWO/CS PM</b>	8.0	2.3	<b>71.4</b>
<b>BWO/CL PM</b>	6.1	1.8	<b>70.5</b>
<b>BWO/CNT PM</b>	5.8	2.6	<b>55.6</b>

## Supporting Information

### Boosting the visible-light photoactivity of $\text{Bi}_2\text{WO}_6$ using acidic carbon additives

Rocio J. Carmona<sup>1</sup>, Leticia F. Velasco<sup>2</sup>, M. Carmen Hidalgo<sup>3</sup>, José A. Navío<sup>3</sup>, Conchi O. Ania<sup>1\*</sup>

<sup>1</sup>ADPOR Group, Instituto Nacional del Carbón (INCAR), Consejo Superior de Investigaciones Científicas (CSIC), Apdo. 73, 33080 Oviedo, Spain

<sup>2</sup>Dpt. Chemistry, Royal Military Academy, Renaissancelaan 30, 1000 Brussels, Belgium

<sup>3</sup>Instituto de Ciencia de Materiales de Sevilla (ICMS), Consejo Superior de Investigaciones Científicas (CSIC) - Universidad de Sevilla, Américo Vespucio 49, 41092 Sevilla, Spain

\*Corresponding author. Tel.: +34 954489550/ +34 985 118846. conchi.ania@incarc.csic.es (CO Ania)

**Figure S1.** Thermal profiles of the carbon materials upon exposure to air at 300°C, showing the effect of the calcination step in the surface chemistry of the carbon additive.

**Figure S2.** Raman spectra of the three carbon materials used as additives.

**Figure S3.** XRD patterns of the carbon additives used, showing the (002) and (10) bands characteristics of the structural order of carbon materials, following the sequence CNT>CL>CS.

**Figure S4.** XRD patterns of pristine sample BWO-CL HS and after irradiation of an aqueous dispersion to explore the stability of the carbon component in the composites (irrad).

**Figure S5.** SEM images and particle size distribution of the carbon materials used as additives.

**Figure S6.** Nitrogen adsorption isotherms at 77K of the bare semiconductors and hybrid composites of the (A) HS series and (B) PM series.

**Figure S7.** XPS data Bi core level of the composites of the HS series.

**Figure S8.** Evaluation of the optical band gap by double linear fitting as the intersection of the extrapolated linear segments of the absorption edge and the photon energy axis in the experimental UV-Vis diffuse reflectance spectra. The double linear fit is a more accurate approach minimizing the fitting error in graphical data integration, as proposed in the literature [Chan et al. Inorg Chem 45 (2006) 8264].

**Figure S9.** Temporal evolution of the UV-vis spectra of RhB aqueous solution upon irradiation of BWO/CS HS, showing the hypsochromic shift characteristic of the formation of N-deethylated intermediates and the fading of RhB concentration after 60 min of irradiation.

**Table S1.** Surface concentration of carbon species obtained by fitting the C 1s core level peak of the XPS spectra of composites BWO-CL and BWO-CS as received (fresh) and after irradiation of an aqueous dispersion to explore the stability of the carbon component.

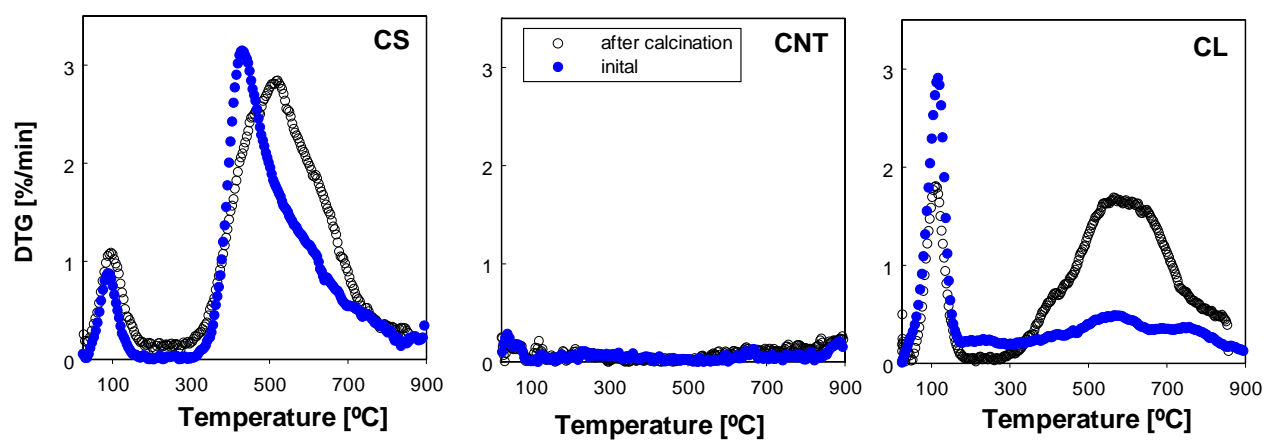


**Figure S1.** Thermal profiles of the carbon materials upon exposure to air at 300°C, showing the effect of the calcination step in the surface chemistry of the carbon additive.

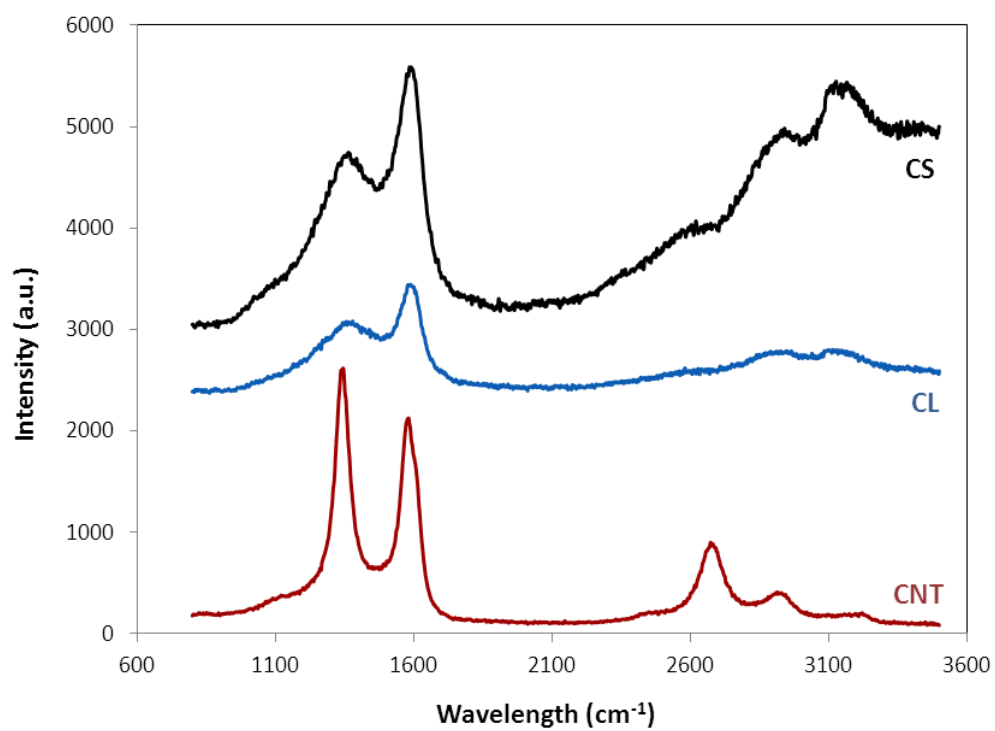


**Figure S2.** Raman spectra of the three carbon materials used as additives.



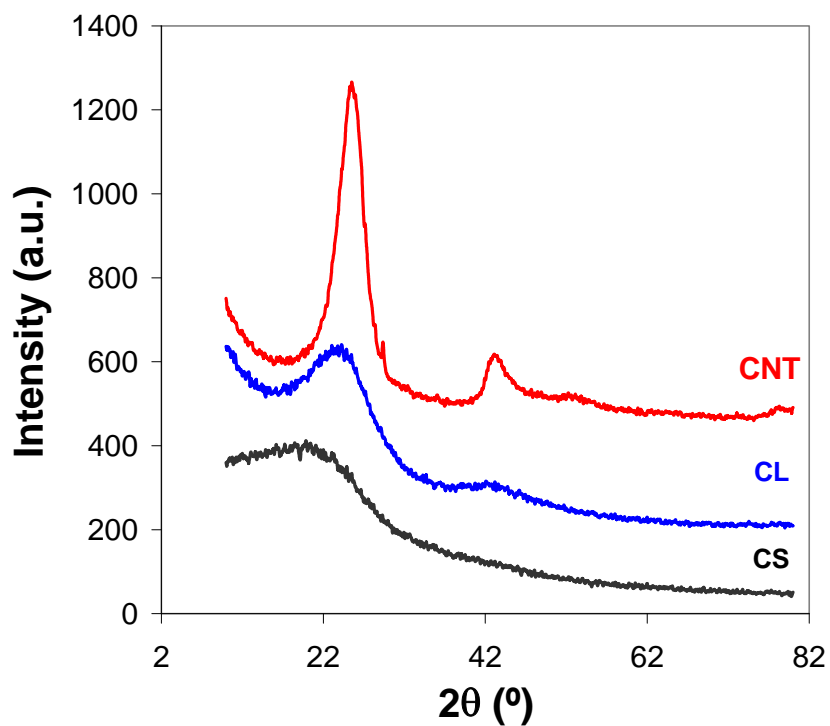


**Figure S3.** XRD patterns of the carbon additives used, showing the (002) and (10) bands characteristics of the structural order of carbon materials, following the sequence CNT>CL>CS.

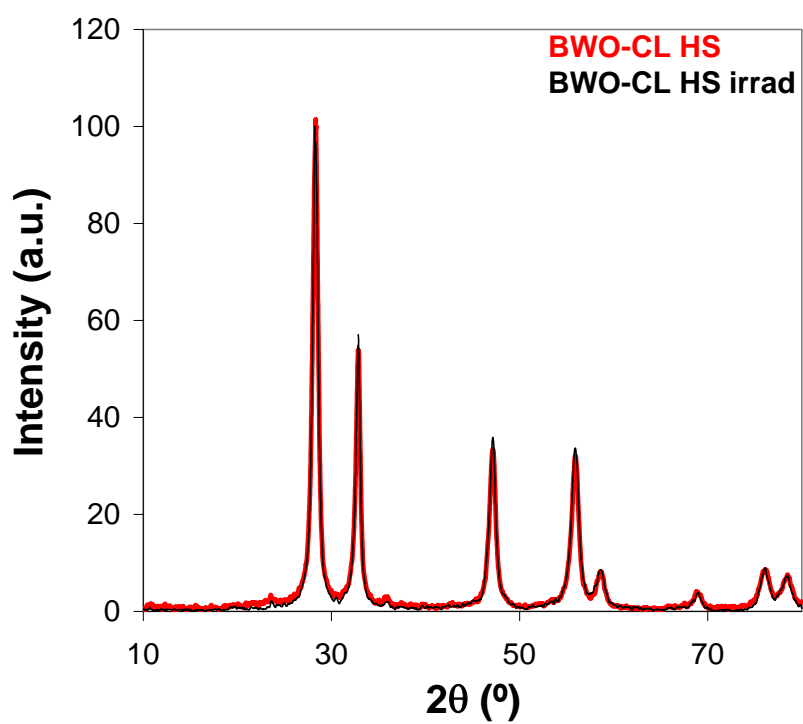


**Figure S4.** XRD patterns of pristine sample BWO-CL HS and after irradiation of an aqueous dispersion to explore the stability of the carbon component in the composites (irrad).

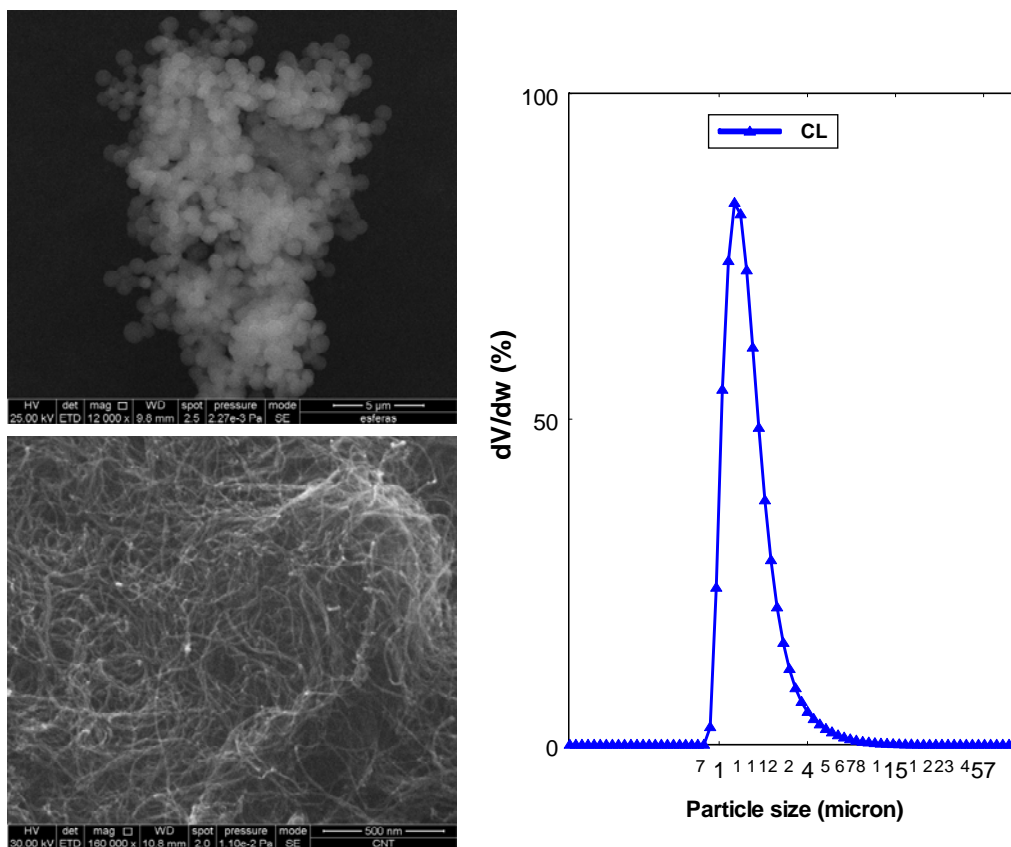


**Figure S5.** SEM images and particle size distribution of the carbon materials used as additives.

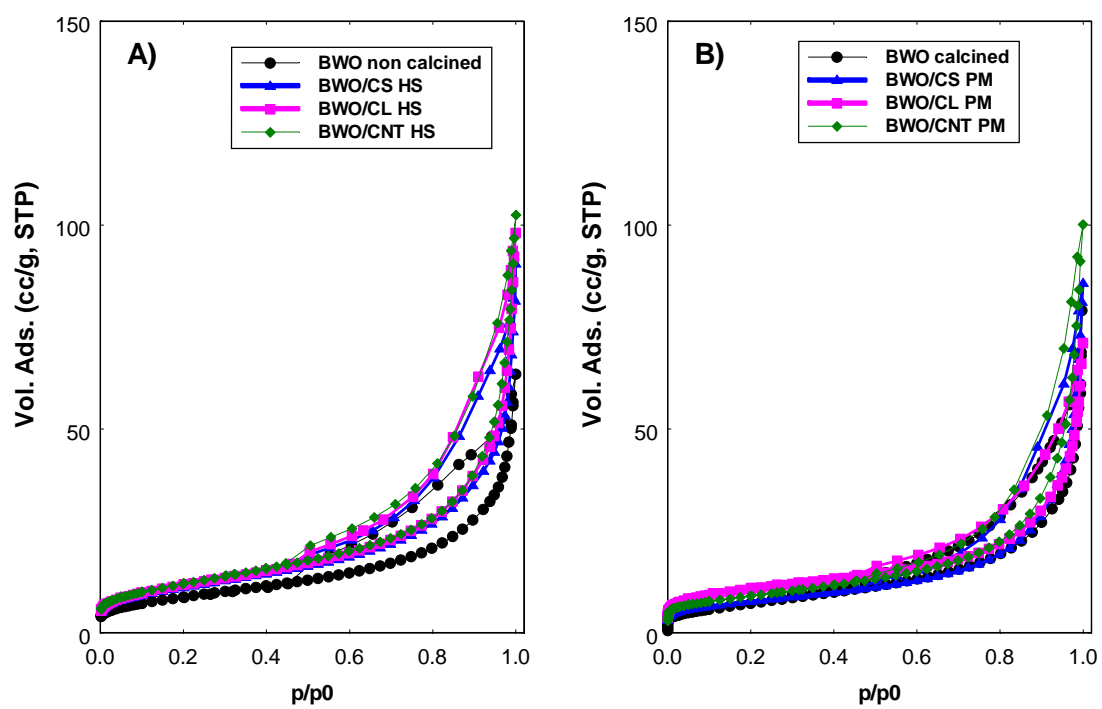


**Figure S6.** Nitrogen adsorption isotherms at 77K of the bare semiconductors and hybrid composites of the (A) HS series and (B) PM series.

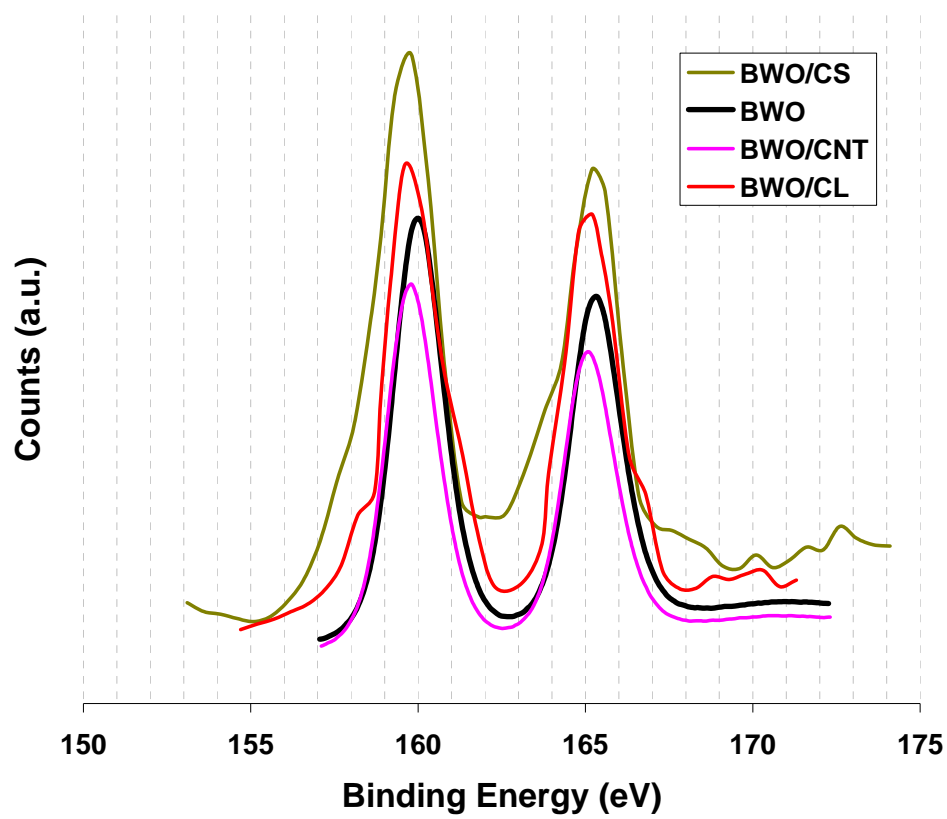


**Figure S7.** XPS data Bi core level of the composites of the HS series.

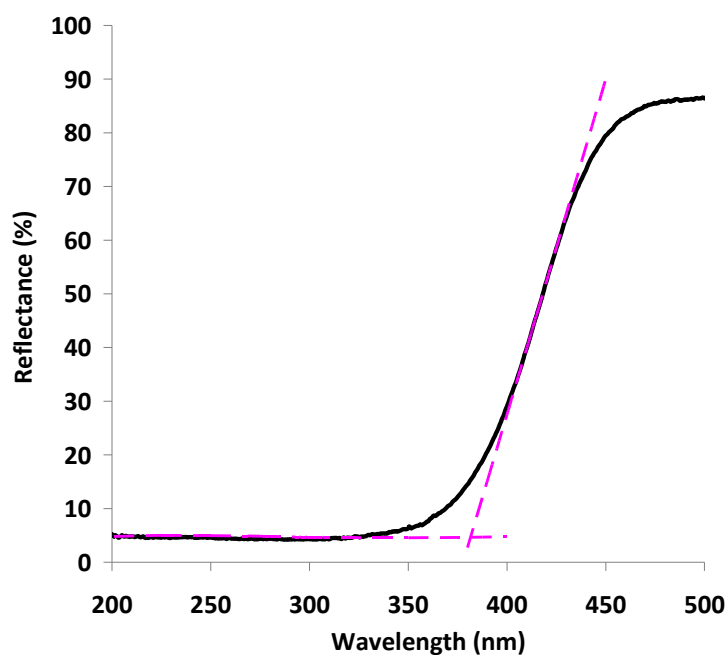


**Figure S8.** Evaluation of the optical band gap by double linear fitting as the intersection of the extrapolated linear segments of the absorption edge and the photon energy axis in the experimental UV-Vis diffuse reflectance spectra. The double linear fit is a more accurate approach minimizing the fitting error in graphical data integration, as proposed in the literature [Chan et al. *Inorg Chem* 45 (2006) 8264].

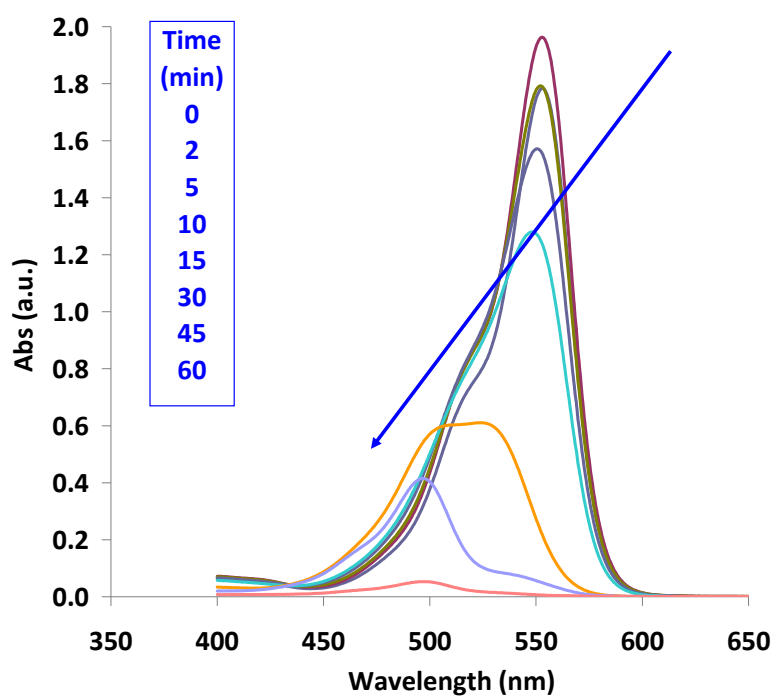


**Figure S9.** Temporal evolution of the UV-vis spectra of RhB aqueous solution upon irradiation of BWO/CS HS, showing the hypsochromic shift characteristic of the formation of N-deethylated intermediates and the fading of RhB concentration after 60 min of irradiation.

**Table S1.** Surface concentration of carbon species obtained by fitting the C 1s core level peak of the XPS spectra of composites BWO-CL and BWO-CS as received (fresh) and after irradiation of an aqueous dispersion to explore the stability of the carbon component.

Bond assignment (energy, eV)	Fresh	irradiated
<b>BWO-CL</b>		
C-C (graphitic carbon - 284.6 eV)	59.3	62.7
C-O (phenolic, alcoholic, etheric - 286.1 eV)	13.8	13.1
C=O (carbonyl or quinone - 287.1 eV)	17.7	18.2
O-C=O (carboxyl or ester - 288.7 eV)	5.8	6.0
$\pi$ - $\pi^*$ (291.0 eV)	3.4	3.5
<b>BWO-CS</b>		
C-C (graphitic carbon - 284.6 eV)	66.5	65.1
C-O (phenolic, alcoholic, etheric - 286.1 eV)	15.9	17.5
C=O (carbonyl or quinone - 287.1 eV)	6.8	7.8
O-C=O (carboxyl or ester - 288.7 eV)	7.5	8.2
$\pi$ - $\pi^*$ (291.0 eV)	3.3	1.3